Numerical estimates for the chemical composition of Enceladus' plume particles

Onni Veteläinen

Supervisors: Nønne Prisle, Jack Lin, Jussi Malila

4.7.2019

University of Oulu
Department of Physics
ATMOS
Master's thesis
763683S

Abstract

The Saturnian moon Enceladus contains a liquid water ocean beneath its surface. Ocean water is released into space through cracks in the moon's frozen crust, forming a plume of vapor and ice-grains. NASA's Cassini mission detected complex organic molecules in these plume particles. The aim of this work is to numerically estimate the chemical composition of the ice-grains found in Enceladus' plume. The ice-grains are assumed to form as bubble bursting aerosols at the ocean surface. Known scaling laws of film and jet drop sizes are combined with a monolayer model of the liquid surface layer, a method which could in principle be applied to any system with bubble bursting aerosols. The bulk ocean water is modeled as an aqueous solution of sodium chloride, sodium carbonate, sodium bicarbonate and slightly soluble organic compounds. The following organic compounds are considered as proxies for the organic compounds present on Enceladus: phenylalanine and its sodium salt as a proxy for an aromatic compound and an amino acid, benzoic acid and benzyl alcohol. The Cassini measurements also imply the existence of very large organic molecules on Enceladus, with molecular masses in excess of 200 u. As a proxy for such compounds we have chosen the humic-like substance Suwannee River Fulvic Acid. Both saturated and supersaturated cases for the organic concentrations are considered. The calculations describe highly enriched organic concentrations for smaller droplets and nearly bulk concentrations for larger ones, as one would expect from surface active compounds. The calculated droplets have lower concentrations of salts than organics, in contrast with Cassini measurements. The calculations could be improved by better estimations of solution surface tension, more sophisticated surface layer characterizations and a better understanding of the bulk ocean composition. Results are also hindered by a poor understanding of the bursting bubble distribution. Future models could account for aerosol dynamics as the droplets rise to the moon' surface.

Contents

Nomenclature

γ	Damping coefficient
δ	Minimum thickness of the pinching region
ϵ	Efficiency of cell puncture
θ_c	Bubble half-cap angle
λ	Wavelength of a capillary wave
λ_0	Characteristic size of a convection cell
μ	Dynamic viscosity
ν	Molecular volume
ξ	Position of a liquid surface
ρ	Density
σ	Surface tension
ϕ	Velocity potential
χ	Mole fraction
ω	Angular frequency
a	Capillary length
Bo	Bond number
d	Film drop diameter
E	Energy
f_0	Appearance frequency of convection cells
g	Gravitational acceleration
h	Thickness of the film cap
h_b	Critical thickness of the film cap
k	Wavenumber

L	Amplitude of a capillary wave
l	Length of the pinching region
l_s	Surface layer thickness
l_μ	Viscous-capillary length
M	Molar mass
m	Mass
Oh	Ohnesorge number
Oh_1	First critical Ohnesorge number
Oh_2	Second critical Ohnesorge number
P	Perimeter of the film cap
p	Pressure
R	Bubble cavity radius
r	Bubble cap radius
R_d	Jet drop radius
R_H	Hinze scale
R_{Bo}	Critical radius corresponding to $Bo = 0.1$
R_{Oh_1}	Critical radius corresponding to Oh_1
S	Surface area of the film cap
t, τ	Time
V	Volume
v, u	Velocity
v_μ	Viscous-capillary speed
w	Mass fraction
x, y, z	Cartesian coordinates

1 Introduction

Saturn's geologically active moon Enceladus contains a liquid water ocean beneath its icy surface [1]. Tidal heating of the porous core sustains the liquid state of the subsurface ocean [2]. Through cracks in the moon's crust, ocean water is released into space [1]. This released material is responsible for the formation of Saturn's E ring [2]. Measurements made by mass spectrometers aboard the Cassini spacecraft show that frozen ice-grains in the plume contain complex organic compounds [2], making Enceladus a very interesting object of study. The origin of these organic compounds, whether primordial or biogenic, is unclear at present. In the primordial scenario the organic carbon on Enceladus would predate the formation of the moon [2]. Over time hydrothermal processes in the core would produce complex organic compounds from simpler precursor molecules [2].

Our aim is to produce numerical estimates for the chemical composition of these plume particles. We suppose that the ice-grains originate as bubble bursting aerosols at the ocean surface, which is a well studied phenomenon on Earth's oceans [3]. On Earth, the bubbles are mostly a result of breaking waves [3]. On Enceladus bubbles of entrapped volatile gases rise through the ocean and burst at the surface [2], resulting in a spray of film drops and the ejection of a drop from a central jet following cavity collapse. We combine known scaling laws of film and jet drop sizes [4, 5] with a characterization of the surface layer [6] to produce estimates of the chemical composition of bubble bursting aerosols on Enceladus.

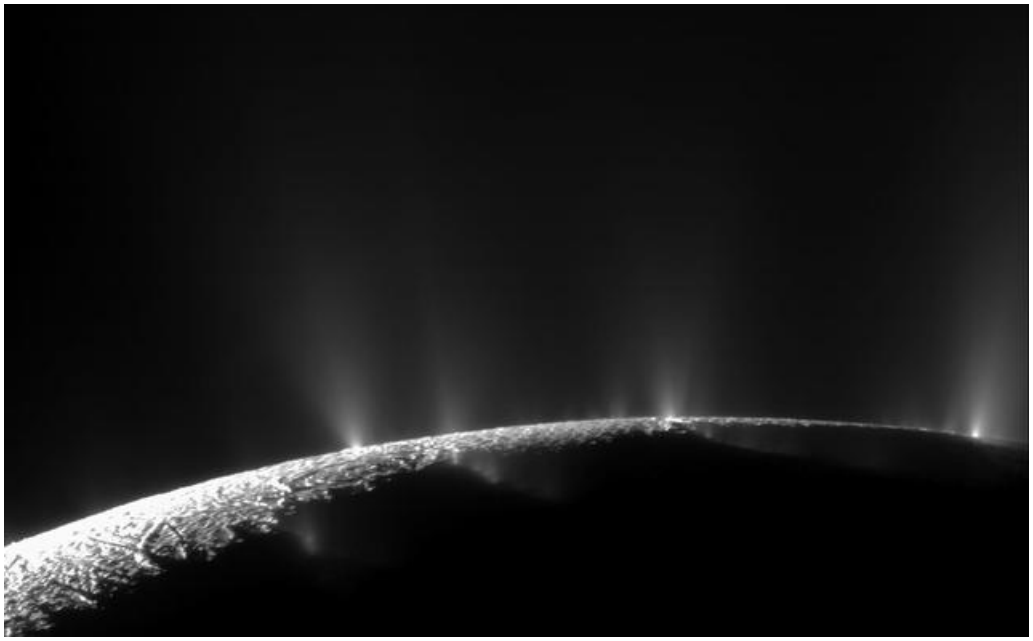

Figure 1: Image taken by the Cassini spacecraft. Water escapes into space through cracks in Enceladus' surface. Credits: NASA/JPL/Space Science Institute

1.1 Enceladus and physical conditions

Enceladus' ocean water is modelled as an aqueous solution of NaCl, $NaHCO_3$, Na_2CO_3 and slightly soluble organic compounds [1]. The concentration of NaCl is $0.05 - 0.2$ molal [1]. Na_2CO_3 and $NaHCO_3$ are found in equal measure, with a combined concentration $0.01 - 0.1$ molal [1]. The pH of the ocean is estimated to be $\sim$ 11-12 [1]. The following organic compounds are considered as proxies for the organic compounds present on Enceladus [2]: phenylalanine and its sodium salt as a proxy for an aromatic compound and an amino acid, benzoic acid and benzyl alcohol. The Cassini measurements also imply the existence of very large organic molecules on Enceladus, with molecular masses in excess of 200 amomic mass units (u) [2]. As a proxy for such compounds we have chosen the humic-like substance Suwannee River Fulvic Acid (SRFA).

Under such high pH conditions phenylalanine, with $pK_a = 9.76$ [7], would be significantly dissociated. At pH = 11 one would expect there to be three times as much sodium phenylalanine than phenylalanine present, and five times as much at pH = 12 [7].

Like Glein et al. in their calculations, we shall consider the temperature at the ocean surface to be at the triple point 0.01 °C, since the liquid ocean and the frozen crust should be in equilibrium [1].

To complete our model of ocean bulk composition we must choose the concentrations of the considered organic compounds. Our first system will be one with saturation concentrations at 0 °C. One possibility for the origin of the organic compounds are chemical processes in the moon's core, where the temperature would be much higher [2]. Our second system will be a supersaturated case, with organic concentrations corresponding to solubilities at 100 °C, assuming that that is the temperature of the ocean-core interface [2].

The gravitational acceleration on Enceladus is 0.113 $\mathrm{m/s^2}$, roughly a percent of that on Earth [8].

2 Theory and background

Two mechanisms for plume particle formation are investigated: film drops and jet drops, both produced by bubble bursting at the ocean-gas interface, analogous to sea spray aerosol formation on Earth [3]. Analysis of film drop formation is given by Lhuissier and Villermaux [4]. Scaling laws of jet drops are given by Gañán-Calvo [5].

Ocean water is modeled as a pseudobinary mixture of an inorganic solution and an organic component, and the surface composition is given by a monolayer partitioning model [6].

2.1 Capillary waves

In this section we will review the theory of capillary waves, following the treatment of Landau and Lifshitz [9]. The dispersion and dissipation of capillary waves will be needed in section 2.2.2 when we consider the formation of jets from bursting bubbles.

Let $\xi(x, y)$ denote the z-coordinate of a liquid surface. At rest the surface is the xy-plane at $z = 0$. If the liquid is perturbed from its equilibrium position, a wave will propagate along the surface under the influence of gravity

and surface tension. Assume that the amplitude L of the wave is small compared to the wavelength λ. Let τ be the oscillation period. During this time the fluid elements will move distances on the order of L, so their velocity will be $v \sim L/\tau$. Fluid elements near the surface will experience acceleration

$$\frac{Dv}{Dt} = \frac{\partial v}{\partial t} + (v \cdot \nabla)v. \tag{1}$$

The velocity of fluid elements in a wave varies over the oscillation period τ and the wavelength λ. Therefore, for the time and spatial derivatives

$$\frac{\partial v}{\partial t} \sim \frac{v}{\tau} \sim \frac{L}{\tau^2}, \tag{2}$$

$$\nabla v \sim \frac{v}{\lambda} \sim \frac{L}{\tau\lambda}. \tag{3}$$

Comparing the two terms, one has

$$\frac{(v \cdot \nabla)v}{\partial_t v} \sim \frac{v^2}{\lambda}\frac{\tau}{v} \sim \frac{v\tau}{\lambda} \sim \frac{L}{\lambda}. \tag{4}$$

Thus, the advective term $(v \cdot \nabla)v$ can be neglected if $L \ll \lambda$, which is what we have assumed. The Euler equation is then

$$\rho\frac{\partial v}{\partial t} = \nabla(-p - \rho g z). \tag{5}$$

Taking the curl of both sides, results in

$$\rho\nabla \times \frac{\partial v}{\partial t} = \rho\frac{\partial \nabla \times v}{\partial t} = 0, \tag{6}$$

since the curl of the gradient is identically zero. This implies that the vorticity $\nabla \times v$ is constant. However, in oscillatory motion, the time average of the velocity should be zero

$$\langle v \rangle = \frac{1}{\tau}\int_0^\tau v dt = 0. \tag{7}$$

Take again the curl of the above equation,

$$\nabla \times \langle v \rangle = \frac{1}{\tau}\int_0^\tau \nabla \times v dt = 0. \tag{8}$$

Since the vorticity is constant and the above integral is zero, the vorticity must be zero.

For any irrotational flow, there exists a velocity potential ϕ from which the velocity can be derived,

$$v = \nabla\phi. \tag{9}$$

Such flows are called potential flows. If a potential flow is incompressible such that $\nabla \cdot v = 0$, it immediately follows that the velocity potential satisfies Laplace's equation

$$\Delta\phi = 0. \tag{10}$$

We have seen that waves of small amplitudes can be approximated as potential flows. Thus we can write Euler's equation as

$$\nabla(\rho\frac{\partial\phi}{\partial t} + p + \rho g\xi) = 0 \tag{11}$$

This implies that the bracketed term is some function $f(t)$ of time only, but this function can be absorbed into ϕ by writing $\phi' = \phi + \int f(t)dt$. This has no physical significance since both ϕ and ϕ' will yield the same velocity field. Therefore we can set $f(t) = 0$ and write

$$p = -\rho g\xi - \rho\frac{\partial\phi}{\partial t}. \tag{12}$$

The pressure in a fluid near the surface is given by the Young-Laplace equation

$$p - p_0 = \sigma\left(\frac{1}{R_1} + \frac{1}{R_2}\right), \tag{13}$$

where σ is the surface tension of the fluid, R_1 and R_2 the principal radii of curvature and p_0 is some constant pressure on the surface, for example the atmosphere. We have assumed that the amplitude of the wave is small, so $\xi(x, y)$ is small as well. For such slightly curved surfaces the bracketed term in equation (13) can be approximated as

$$\frac{1}{R_1} + \frac{1}{R_2} = -\left(\frac{\partial^2\xi}{\partial x^2} + \frac{\partial^2\xi}{\partial y^2}\right). \tag{14}$$

Combining equations (12), (13) and (14), we have that

$$\rho\frac{\partial\phi}{\partial t} + \rho g\xi - \sigma\left(\frac{\partial^2\xi}{\partial x^2} + \frac{\partial^2\xi}{\partial y^2}\right) = 0, \tag{15}$$

where we have gotten rid of p_0 by again redefining ϕ as $\phi - p_0 t/\rho$. As an approximation, suppose that z-component of velocity near the surface is just the time derivative of ξ,

$$v_z = \frac{\partial \phi}{\partial z} = \frac{\partial \xi}{\partial t}. \tag{16}$$

Take the time derivative of (15),

$$\begin{aligned} &\rho \frac{\partial^2 \phi}{\partial t^2} + \rho g \frac{\partial \xi}{\partial t} - \sigma \frac{\partial}{\partial t}\left(\frac{\partial^2 \xi}{\partial x^2} + \frac{\partial^2 \xi}{\partial y^2} \right) = 0 \\ \Rightarrow &\rho \frac{\partial^2 \phi}{\partial t^2} + \rho g \frac{\partial \xi}{\partial t} - \sigma \left(\frac{\partial^2}{\partial x^2}\frac{\partial \xi}{\partial t} + \frac{\partial^2}{\partial y^2}\frac{\partial \xi}{\partial t} \right) = 0 \\ \Rightarrow &\rho \frac{\partial^2 \phi}{\partial t^2} + \rho g \frac{\partial \phi}{\partial z} - \sigma \left(\frac{\partial^2}{\partial x^2}\frac{\partial \phi}{\partial z} + \frac{\partial^2}{\partial y^2}\frac{\partial \phi}{\partial z} \right) = 0, \quad z = 0. \end{aligned} \tag{17}$$

The potential ϕ must now satisfy Laplace's equation (10) with the boundary condition (17). Consider a plane wave propagating along the x-axis. Solutions are of the form $\phi = f(z)\cos(kx - \omega t)$, where k is the wave number and ω the angular frequency.

$$\begin{aligned} &\frac{\partial^2 \phi}{\partial x^2} + \frac{\partial^2 \phi}{\partial z^2} = 0 \\ \Rightarrow &-k^2 \cos(kx - \omega t) + \frac{\partial^2 f(z)}{\partial z^2}\cos(kx - \omega t) = 0 \\ \Rightarrow &\frac{\partial^2 f(z)}{\partial z^2} = k^2 f(z). \end{aligned} \tag{18}$$

The solution is either $f(z) = Ae^{kz}$ or Ae^{-kz}. We choose $f(z) = Ae^{kz}$, since the velocity potential must diminish inside the fluid. The dispersion relation is obtained from the boundary condition (17) by inserting $\phi = Ae^{kz}\cos(kx - \omega t)$,

$$\begin{aligned} \rho \frac{\partial^2 \phi}{\partial t^2} + \rho g \frac{\partial \phi}{\partial z} - \sigma \left(\frac{\partial^2}{\partial x^2}\frac{\partial \phi}{\partial z} + \frac{\partial^2}{\partial y^2}\frac{\partial \phi}{\partial z} \right) &= 0 \\ \Rightarrow \rho g k - \rho \omega^2 - \sigma(-k^3 + 0) &= 0 \\ \Rightarrow \omega^2 = gk + \frac{\sigma}{\rho}k^3. & \end{aligned} \tag{19}$$

Comparing the two terms on the right in equation (19), one obtains the dimensionless Bond number $Bo = \rho g \lambda^2/\sigma$ for the wave,

$$\frac{gk}{k^3\sigma/\rho} = \frac{g\rho}{k^2\sigma} = \frac{\rho g \lambda^2}{\sigma}, \tag{20}$$

where the wavelength λ is taken to be the characteristic length of the system. Thus the Bond number compares gravitational and surface tension forces. If $Bo \ll 1$, gravitational effects can be neglected and the wave is called a capillary wave. If $Bo \gg 1$, the surface tension term is negligible and we have gravity waves. Intermediate cases, $Bo \approx 1$, are called capillary gravity waves.

For capillary waves the dispersion relation becomes $\omega^2 = \sigma k^3/\rho$, and the propagation speed of the wave is

$$\frac{\partial \omega}{\partial k} = \frac{3}{2}\left(\frac{\sigma k}{\rho}\right)^{1/2}. \tag{21}$$

2.1.1 Viscous dissipation

The energy dissipation due to internal friction in an incompressible flow is

$$\dot{E} = -\frac{1}{2}\mu \int \left(\frac{\partial v_i}{\partial x_k} + \frac{\partial v_k}{\partial x_i}\right)^2 dV, \tag{22}$$

where μ is the dynamic viscosity of the fluid. Note that we are here assuming that the viscosity is uniform. This is not necessarily true in the presence of surfactants, which may introduce a vertical viscosity gradient. Now, for a potential flow $\partial v_i/\partial x_k = \partial^2\phi/\partial x_k \partial x_i = \partial v_k/\partial x_i$, so

$$\begin{aligned} \dot{E} &= -\frac{1}{2}\mu \int \left(2\frac{\partial v_i}{\partial x_k}\right)^2 dV = -2\mu \int \left(\frac{\partial^2 \phi}{\partial x_i \partial x_k}\right)^2 dV \\ &= -2\mu \int (-k^2 \sin(kx - \omega t) A e^{kz})^2 dV \\ &= -2\mu k^4 \int A^2 e^{2kz} \sin^2(kx - \omega t) dV, \end{aligned} \tag{23}$$

the time average of which is

$$\langle \dot{E} \rangle = -2\mu k^4 \int \langle \phi^2 \rangle \, dV, \tag{24}$$

since

$$\langle \phi^2 \rangle = A^2 e^{2kz} \left\langle cos^2(kx - \omega t) \right\rangle, \tag{25}$$

and $\langle \sin^2(kx - \omega t) \rangle = \langle \cos^2(kx - \omega t) \rangle$. For any periodic motion with a small amplitude, the average kinetic and potential energies are equal, so the mean

total mechanical energy of the system can be written as twice the mean kinetic energy

$$\begin{aligned}\langle E\rangle &= \rho\int \langle v^2\rangle\, dV = \rho\int \langle(\nabla\phi)^2\rangle\, dV \\ &= \rho\int k^2\left\langle \sin^2(kx-\omega t)\right\rangle A^2e^{2kz} + k^2\left\langle\cos^2(kx-\omega t)\right\rangle A^2e^{2kz}dV \\ &= 2\rho k^2\int\langle\phi^2\rangle\, dV.\end{aligned} \tag{26}$$

We define the damping coefficient γ as the ratio of the energy dissipation and total energy

$$\gamma = \frac{|\langle\dot{E}\rangle|}{\langle E\rangle} = \frac{\mu k^2}{\rho}, \tag{27}$$

which has units of time^{-1}. We may define another dimensionless number by multiplying the damping coefficient by a characteristic timescale τ of the system. A natural choice in this case is the time it takes for the wave to propagate the distance one wavelength. For a capillary wave with a propagation speed $v \sim (\sigma k/\rho)^{1/2}$, we have

$$\gamma\tau = \frac{\gamma\lambda}{v} = \frac{\mu}{\rho\lambda^2}\frac{\lambda^{3/2}\rho^{1/2}}{\sigma^{1/2}} = \frac{\mu}{\sqrt{\rho\sigma\lambda}}. \tag{28}$$

Equation (28) defines the Ohensorge number $Oh = \mu/\sqrt{\rho\sigma\lambda}$ of the system, with the wavelength λ being here the characteristic length of the system. The motion of the wave is driven by surface tension forces and is dissipated by viscosity. The Ohnesorge number compares the viscous forces with the capillary forces, and if $Oh \gg 1$, the wave will be damped very rapidly. If $Oh \approx 1$, then the wave will be damped over a distance of one wavelength, and if $Oh \ll 1$ then the wave may propagate distances much larger than one wavelength before being dissipated.

2.2 Dynamics of bubble bursting

Bubble bursting at a liquid surface produces two kinds of aerosols. After a bubble bursts, the rippling film cap breaks up into a large number of droplets called film drops [4]. Capillary waves then travel down the exposed bubble cavity, colliding in the centre and producing a rising jet of liquid, which may break up into jet drops [5]. Jet drops are generally less numerous than films drops [3].

Bubble bursting is an important physical process, as the resulting aerosols provide a mechanism of material and heat exchange between the ocean and the atmosphere [3]. On Earth the droplets regulate atmospheric chemistry, global radiation balance and the water cycle [10].

The chemical composition of smaller droplets may differ significantly from the bulk composition if surface-active compounds are present [3], as is the case on Enceladus. In this section we will review the theory of bubble bursting and the resulting droplet production, with the most important results being the formulae of droplet radii as functions of the bursting bubble radius [4][5]. In section 3 we will combine this knowledge with the monolayer model [6] reviewed in section 2.3 to produce estimations of the composition of Enceladus' plume particles.

2.2.1 Film drop production

The analysis of film drop production is given by Lhuissier and Villermaux in their 2011 paper [4]. In this section we will review the steps taken to arrive at the scaling law for average drop size.

Figure 2: Diagram of a bubble at a liquid interface

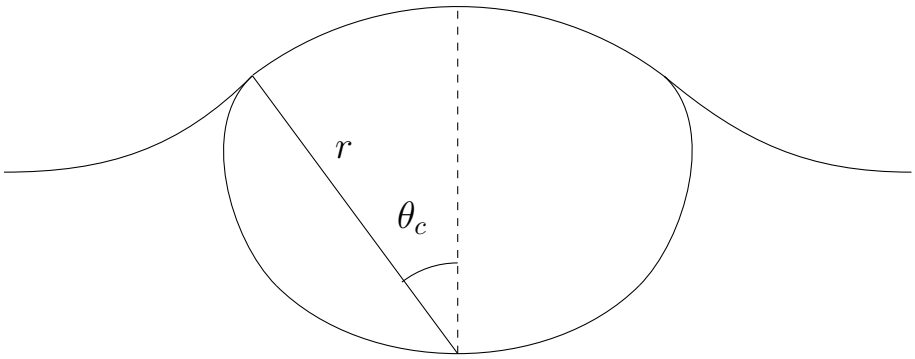

Consider first a submerged bubble at the liquid surface. The bubble profile will consist of three regions; the cavity surface with radius of curvature R, the bubble cap with radius of curvature r, and the meniscus where the cap connects to the liquid bulk, see figure 2. The cavity radius is required to be half the cap radius, due to the cap having two interfaces instead of one, like the cavity surface. We will assume that the density of the entrapped gas ρ_0 is negligible compared to that of the surrounding liquid ρ, such that

$\rho - \rho_o \approx \rho$. Then due to gravity, the bubble experiences a buoyancy

$$\rho g \frac{4\pi}{3} \left(\frac{r}{2}\right)^2, \tag{29}$$

which is opposed by the vertical component of surface tension acting on the rim of the bubble cap

$$2\pi r \sigma \sin^2 \theta_c. \tag{30}$$

The bubble comes to rest when the two forces are equal. From this one can obtain for the half-cap angle θ_c

$$\sin \theta_c = \sqrt{\frac{\rho g}{\sigma}} \frac{r}{2\sqrt{3}} = \frac{r}{2\sqrt{3}a} = \frac{\sqrt{Bo}}{2\sqrt{3}}, \tag{31}$$

where $a = \sqrt{\sigma/\rho g}$ is the capillary length and the Bond number $Bo = \rho g r^2/\sigma = (r/a)^2$ again compares the gravitational and surface tension forces. If Bo is sufficiently small, one can approximate θ_c as

$$\theta_c = \frac{\sqrt{Bo}}{2\sqrt{3}}, \tag{32}$$

which holds up to $Bo = 25$ [4]. Since gravity and surface tension are the only forces acting on the bubble, it is not surprising that the bubble geometry is defined by the Bond number. In the limit of $Bo \to 0$ the bubble becomes completely submerged and spherical, resting just below the surface. In such a case one would not expect any film drops to form, since no film cap exists. Therefore there should exist some critical Bond number below which no film drops are produced.

Once the bubble is at rest, gravity causes a surfactant concentration gradient and thus a surface tension gradient to form, holding up the film cap [4]. The pressure inside the cap is the sum of capillary pressure, due to the Young-Laplace equation (13), and hydrostatic pressure. The capillary pressure will dominate in the case of $Bo < 25$ [4]. The pressure difference between the meniscus and the film interior is the capillary pressure $2\sigma/\rho$, which drives the draining flow u, from the film to the meniscus. This flow creates a pinching region at the perimeter of the film cap, with length l and minimum thickness δ [4], see figure 3. The flow is in the interior of the film, between two mobile layers of surfactants. For a steady flow, one has

$$\rho \frac{Du}{Dt} = -\nabla p + \mu \nabla^2 u = 0. \tag{33}$$

Figure 3: Diagram of the pinching region

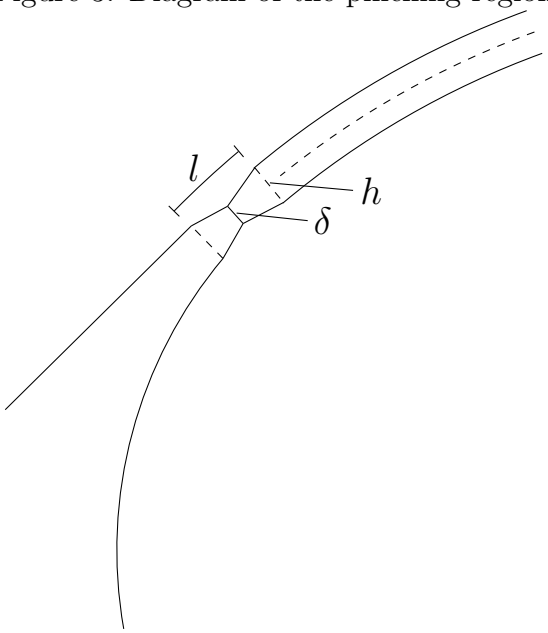

The pressure difference $2\sigma/r$ is over the length l. Assuming no-slip at the film interfaces, the velocity changes over the distance δ. Then in orders of magnitude

$$\frac{\sigma}{rl} \sim \frac{\mu u}{\delta^2}. \tag{34}$$

The curvature in the pinching region should match the cap curvature [4]

$$\frac{h-\delta}{l^2} \sim \frac{1}{r}. \tag{35}$$

At the same time an opposite flux exists in the surface layer. Convective motion is induced over the pinching region due to destabilization caused by the surface tension difference [4]. This phenomenon is called *marginal regeneration*, and it regulates the pinching region such that the neck thickness δ never becomes smaller than half the film cap thickness h.

Now, from (34) we have that

$$u \sim \frac{\sigma\delta^2}{rl\mu}, \tag{36}$$

and from (35)

$$l \sim \sqrt{r(h-\delta)} \sim \sqrt{rh}. \tag{37}$$

Therefore the drainage velocity

$$u \sim \frac{\sigma\delta^2}{r\sqrt{rh}\mu} = \frac{\sigma h^2}{\mu r^{3/2}h^{1/2}} = \frac{\sigma}{\mu}\left(\frac{h}{r}\right)^{3/2}. \tag{38}$$

The liquid drains from the film cap with thickness h and surface area S, through the cap perimeter P. From mass conservation, one has for the interior flow

$$\dot{h} \sim -hu\frac{P}{S}. \tag{39}$$

The surface area of the cap

$$S = 2\pi r^2(1-\cos\theta_c) \approx \pi r^2\theta_c^2, \tag{40}$$

and the perimeter

$$P = 2\pi r\sin\theta_c \approx 2\pi r\theta_c, \tag{41}$$

where the small-angle approximations have been used. The ratio P/S is then

$$\frac{P}{S} \sim \frac{2\pi r\theta_c}{\pi r^2\theta_c^2} = \frac{2}{r\theta_c}. \tag{42}$$

From (32), (38), (39) and (42), we have that

$$\dot{h} \sim -hu\frac{2}{r\theta_c} \sim -\frac{\sigma a h^{5/2}}{\mu r^{7/2}}, \tag{43}$$

which is a separable differential equation. Separating and integrating (43), we get a thinning law for the film thickness

$$h \sim \left(\frac{\mu r^{7/2}}{\sigma a t}\right)^{2/3}. \tag{44}$$

Convection cells from marginal regeneration appear at a frequency [4]

$$f_0 \sim \frac{\sigma}{\mu a}\left(\frac{r}{a}\right)^{1/3}\left(\frac{\mu a}{\sigma t}\right)^{2/3}, \tag{45}$$

and have a characteristic size [4]

$$\lambda_0 \sim r\left(\frac{h}{r}\right)^{3/2}. \tag{46}$$

It has been observed that film puncture happens near the cap foot, in the centre of these convection cells [4]. However this process is seen to be inefficient; Lhuissier and Villermaux propose $\epsilon \sim O(10^{-4} - 10^{-3})$ as the efficiency of cell puncture, such that the probability of puncture in a cell within a time interval δt is $\epsilon f_0 \delta t$. The probability $p(t)$ of a puncture somewhere on the surface is then proportional to ϵ and the number of cells, which is $\sim P/\lambda_0$,

$$p(t)\delta t \sim \epsilon \frac{P}{\lambda_0} f_0 \delta t. \tag{47}$$

Using equations (41), (45), (46) and defining

$$\tau_0 = \frac{(4/3)^{3/4}}{\epsilon^{3/4}} \frac{\mu a}{\sigma} \left(\frac{r}{a}\right)^{1/2}, \tag{48}$$

we write the probability $p(t)$ as

$$p(t) = \frac{4}{3} \frac{t^{1/3}}{\tau_0^{4/3}}. \tag{49}$$

If the bubble has not burst from time $t = 0$ to some time t, it must not have burst on subsequent time intervals $\delta t'$ from 0 to t. The probability of no puncture is

$$Q(t) = \prod_{t'/\delta t'=0}^{t/\delta t'} [1 - p(t')\delta t'], \tag{50}$$

which becomes

$$Q(t) = \exp\big(-\int_0^t p(t')dt'\big) \tag{51}$$

and in the limit of $\delta t \to 0$. The mean bubble lifetime is [4]

$$t_b = \int_0^\infty Q(t)dt = \Gamma(7/4)\tau_0 \approx 0.92\tau_0. \tag{52}$$

With the thinning law (44) and the above mean lifetime, one has the film thickness at time of bursting

$$h_b \sim \left(\frac{\mu r^{7/2}}{\sigma a \tau_0}\right)^{2/3} = a\epsilon^{1/2}\left(\frac{r}{a}\right)^2 = a\epsilon^{1/2} Bo. \tag{53}$$

After puncture the nucleated hole is expanded by surface tension with a velocity $v = \sqrt{2\sigma/\rho h}$ [4]. The rim recedes following the film curvature and

experiences a destabilization which causes ligaments to form at the edge of the rim. Ligaments are spaced by the instability wavelength $\lambda \sim \sqrt{rh}$ [4] and they form with a growth time $\tau \sim \sqrt{\rho(rh)^{3/2}/\sigma}$ [4]. The ligaments then break up into film drops, and their diameter is set by the ligament diameter at breakup. The ligament diameter is seen to remain constant from the moment of formation τ, since their stretching is compensated by flow from the film [4]. The average ligament and thus drop diameter is proportional to the rim diameter at the time of ligament formation τ [4]

$$\langle d \rangle \sim \sqrt{v\tau h_b} \sim r^{3/8} h_b^{5/8}. \tag{54}$$

As a crude approximation, the number of film drops produced can be estimated by assuming the entire volume of the film cap $\sim Sh_b$ is formed into film drops with volume $\sim \langle d \rangle^3$,

$$\langle N \rangle \sim \frac{Sh_b}{\langle d \rangle^3} \sim \frac{r^2 h_b Bo}{r^{9/8} h_b^{15/8}} = Bo\left(\frac{r}{h_b}\right)^{7/8}. \tag{55}$$

For film drops to form, the recession time of the rim $\sim r\theta_c/V$ must be larger than the growth time τ and the ejection time $\sim 3\tau$ [4]. In the limiting case

$$\begin{aligned} \sqrt{\frac{\rho(rh_b)^{3/2}}{\sigma}} &\sim r\theta_c/v \sim r\sqrt{Bo}/\sqrt{2\sigma/\rho h_b} \\ Bo &\sim \frac{\rho r^{3/2} h_b^{3/2} \sigma}{\sigma r^2 \rho h_b} = \left(\frac{h_b}{r}\right)^{1/2} \\ Bo &\sim (Bo\epsilon)^{1/4} \\ Bo &\sim \epsilon^{1/3}, \end{aligned} \tag{56}$$

and since $\epsilon \sim 10^{-3}$, we have the Bond number below which no film drops should form

$$Bo \sim O(10^{-1}). \tag{57}$$

2.2.2 Jet drop production

Once the bubble cap has burst, capillary waves will travel down the exposed cavity, colliding at the axis of symmetry and forming an upwards liquid jet.

A scaling law for the ejected jet drop is given by Gañán-Calvo [5]. The collapsing capillary waves have a propagation speed v_0 given by the equation (21), and experience viscous dissipation from the equation (27) as they travel down the cavity. Assuming that the wavelength λ of the capillary waves is proportional to the cavity radius R [5], we have that

$$\begin{aligned} \lambda = 1/k &\sim R \\ v_0 &\sim \left(\frac{\sigma}{\rho R}\right)^{1/2} \end{aligned} \tag{58}$$

The length travelled by the capillary wave is proportional to R, so its propagation rate is $\tau_c^{-1} \sim v_0/R \sim \left(\frac{\sigma}{\rho R^3}\right)^{1/2}$. The dissipation rate from equation (27) is $\gamma \sim \frac{\mu}{\rho R^2}$. In order to form a jet and eject a drop, the wave must not be completely dissipated before it reaches the bottom of the cavity. In other words, the propagation rate must be larger than the dissipation rate

$$\begin{aligned} \tau_c^{-1} &> \gamma \\ \tau_c \gamma &< 1. \end{aligned} \tag{59}$$

We have the Ohnesorge number from equation (28)

$$Oh = \gamma \tau_c = \frac{\mu}{\sqrt{\rho \sigma \lambda}} < 1. \tag{60}$$

The Ohnesorge number must be at the very least less than one. However, at the time of collapse the wave must still have significant energy left to eject a drop, and the actual critical Ohnesorge number has been experimentally determined to be $Oh_1 = 0.038$ [5]. The Ohnesorge number of the system must be lower than Oh_1 to eject a jet drop.

Figure 4: Diagram of jet formation

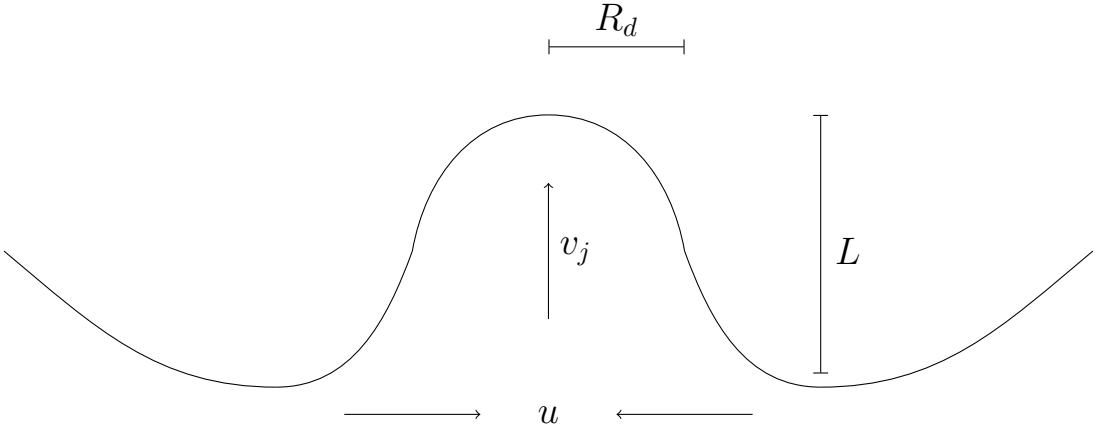

Let us identify characteristic speeds and length scales at the moment of collapse. Let the eventual drop radius R_d be the radial length and the amplitude of the wave L the axial length. Let u be the radial speed in the surface layer and the launch speed of the jet v_j the axial speed. See figure 4.

Now, the drop is seen to be ejected at a height comparable to R, so the jet requires a kinetic energy $\sim \rho R R_d^2 v_j^2$ to eject a drop [5]. The energy available to the jet is the surface energy of the ruptured film cap $\sim \sigma S$, the gravity potential imbalance of the cavity proportional to its height and volume $\sim (\rho g R) R^3$, and the negative contribution of the viscous dissipation $\sim \mu(\sigma R^3/\rho)^{1/2}$. Thus we have the energy balance

$$Oh_1 \sigma R^2 + k_{Bo,1} \rho g R^4 - \mu(\sigma R^3/\rho)^{1/2} \sim k' \rho R R_d^2 v_j^2, \tag{61}$$

where $k_{Bo,1}$ and k' are fitting parameters [5]. There is also the negative contribution from gravity acting on the rising jet, but this is negligible, since the volume of the jet is much smaller than that of the cavity.

For the momentum balance we have the observation that maximum velocity takes place just after collapse, as the jet is about to form [5]. Therefore at the moment of jet ejection we have near zero stress for a fluid element at the surface near the axis

$$\rho \frac{\partial v}{\partial t} + \rho(v \cdot \nabla) v = -\nabla p + \mu \nabla^2 v \sim 0, \tag{62}$$

and thus all four terms should be comparable to each other. In orders of magnitude

$$\rho v_j^2 / L \sim \sigma / R_d^2 \sim \mu u / L^2. \tag{63}$$

Considering a cylindrical control volume at the point of collapse, with radius R_d and height L. One has from mass conservation

$$u L R_d \sim v_j R_d^2, \tag{64}$$

since we are assuming an incompressible flow. From equations (63) and (64)

$$\begin{aligned} R_d/l_\mu &\sim (u/v_\mu)^{-5/3}, \\ L/l_\mu &\sim (u/v_\mu)^{-4/3}, \\ v_j/v_\mu &\sim (u/v_\mu)^{2/3}, \end{aligned} \tag{65}$$

where $v_\mu = \sigma/\mu$ and $l_\mu = \mu^2/\rho\sigma$ are the viscous-capillary speed and length, respectively [5].

The above scaling laws (65) should hold for any capillary wave collapsing at the cavity bottom, and it is seen that faster but smaller wave collide before a slower but larger wave, with $\lambda \sim R$, produces a jet. Gañán-Calvo proposes that the radial speed u is induced by the capillary waves through viscous effects and the inertial push of the largest wave [5]

$$\rho u^2 \sim \mu v_c / L + Oh_2 \rho v_0^2, \tag{66}$$

where Oh_2 is a second critical Ohnesorge number signifying the inviscid limit, below which the inertial push of the largest wave will dominate. The value of Oh_2, is experimentally determined to be $Oh_2 = 0.0045$ [5].

Now, combining equations (61), (65) and (66), one has the scaling law for the ejected drop radius [5]

$$\frac{R_d}{l_\mu} \sim \frac{[Oh^{-1}\left(\frac{Oh_1}{Oh} - 1 + k_{Bo,1}\frac{Bo}{Oh}\right)]^{5/4}}{\left(1 + \frac{Oh_2}{Oh}\right)^{1/2}} \equiv \phi_R, \tag{67}$$

$$\frac{R_d}{l_\mu} = k_d \phi_R, \tag{68}$$

where the fitting parameters $k_{Bo,1} = 0.006$ and $k_d = 0.9$ [5].

2.3 The monolayer model

In order to compute the chemical composition of the produced aerosols, one has to know the composition and thickness of the surface layer. The tools to estimate these are provided by Malila and Prisle [6].

Let $\chi^b = (\chi_1^b, \chi_2^b, ..., \chi_i^b)$ be the composition of the liquid bulk, where χ_i^b are the mole fractions of the constituent compounds of the solution. Let χ^s be the corresponding surface layer composition. Let σ_i be the surface tension of the pure compounds i that make up the solution, and ν_i their molecular volumes. The surface tension of a droplet, with surface layer of thickness l_s, is given by the following semiempirical formula [6]

$$\sigma(\chi^b) = \frac{\Sigma_i \sigma_i \nu_i \chi_i^s}{\Sigma_i \nu_i \chi_i^s}, \tag{69}$$

and the surface layer thickness by [6]

$$l_s = \left(\frac{6}{\pi} \sum_i \nu_i \chi_i^s\right)^{1/3}. \tag{70}$$

The molecular volumes of the components are calculated from their molar masses M_i and densities ρ_i as

$$\nu_i = \frac{M_i}{\rho_i N_A}, \tag{71}$$

where N_A is the Avogadro constant.

The solution of surface composition χ^s from equation (69) using pseudobinary approximations will be covered in section 3.

3 Calculations and results

3.1 Calculations

Using the tools reviewed in the last section, we can estimate the chemical composition Enceladus' plume particles in terms of mass fractions. The calculations are carried out in MATLAB.

We take as input the liquid bulk composition χ^b and the radius of the bursting bubble. To start out, we can estimate the surface tension σ_m and viscosity μ_m of a mixture using the following mixing formulas [11], for the surface tension

$$\ln \sigma_m = \sum_i \chi_i^b \ln \sigma_i, \tag{72}$$

and the viscosity

$$\mu_m = \prod_i \mu_i^{\chi_i^b}. \tag{73}$$

See Appendix A for a complete description of the component and mixture surface tensions, viscosities and densities.

From the bubble radius R, by which we here mean the cavity radius, we can calculate the capillary length $a = \sqrt{\sigma/\rho g}$, the viscous-capillary length $l_\mu = \mu^2/\rho\sigma$, the Ohnesorge number $Oh = \mu/\sqrt{\rho\sigma R}$ and the Bond number $Bo = \rho g R^2/\sigma$. With these values the radius r of the produced droplets is calculated either from the equation (54) or the equation (68), depending on the Bond number. For film drop formation it is required that $Bo > 0.1$, and since the number of film drops generated is in general much larger than the number of jet drops, we will neglect jet drop formation in this region. The volume of the droplet is of course

$$V_d = \frac{4}{3}\pi r^3, \tag{74}$$

and with the thickness of the surface layer from equation (70), the volume of the surface layer is

$$V_s = V_d - V_b, \tag{75}$$

where the droplet bulk volume V_b is

$$V_b = \frac{4}{3}\pi(r - l_s)^3. \tag{76}$$

Now we must acquire the surface layer composition χ^s from equation (69). We are considering a system with water and four components, and we cannot simultanously solve five numbers from one equation. For two components however, the equation can be solved as

$$\chi_2 = \frac{\nu_1\sigma_1 - \sigma\nu_1}{\sigma(\nu_2 - \nu_1) + \nu_1\sigma_1 - \nu_2\sigma_2}, \tag{77}$$

since $\chi_1 = 1 - \chi_2$. We will use a pseudobinary approximation, where we consider the system to be a mixture of only two components [6], the organic part χ_{org} and salt water $\chi_{sw} = \chi_w + \chi_2 + \chi_3 + \chi_4$. The molecular volume of the pseudobinary salt water is approximated as [6]

$$\nu_{sw} = \frac{\sum_i \bar{\chi}_i^b M_i}{\rho_{sw}}, \tag{78}$$

where $\bar{\chi}_i^b = \chi_i^b / \Sigma_j \chi_j^b$ are the pseudobinary salt water mole fractions, and the sums are over the components of the pseudobinary mixture, including water. The salt water density ρ_{sw} is again given in appendix A.

The surface mole fraction for the organic compound is then

$$\chi_{org} = \frac{\nu_{sw}\sigma_{sw} - \sigma_m\nu_{sw}}{\sigma_m(\nu_{org} - \nu_{sw}) + \nu_{sw}\sigma_{sw} - \nu_{org}\sigma_{org}}, \tag{79}$$

where σ_m is the surface tension of the mixture and σ_{sw} the surface tension of salt water. The rest of the mole fractions are solved one at a time using further pseudobinary approximations, taking one of the salts on its own and having the rest make up a new pseudobinary mixture.

Having calculated the droplet bulk and surface volumes V_b and V_s, and the surface composition χ^s, we get the mass of the organic compound in the surface layer

$$m_{org}^s = w_{org}^s m_s, \tag{80}$$

where $w^s_{org} = \chi^s_{org} M_{org} / \Sigma_i \chi^s_i M_i$ is the mass fraction of the organic compound in the surface layer, and $m_s = V_s \rho_s$ is the total mass of the surface layer. Similarly for the droplet bulk, we have

$$m^b_{org} = w^b_{org} m_b, \tag{81}$$

with $w^b_{org} = \chi^b_{org} M_{org} / \Sigma_i \chi^b_i M_i$ and $m_b = V_b \rho_b$. The mass fraction of the organic compound in the entire droplet is then

$$w_{org} = \frac{m^s_{org} + m^b_{org}}{m_d}, \tag{82}$$

where $m_d = m_s + m_b$ is the total mass of the droplet.

3.1.1 Relevant bubble sizes

Assuming that the viscosity, surface tension and gravitational acceleration can be considered as being roughly constant during the bubble bursting process, the Bond and Ohnesorge numbers become essentially functions of the bubble radius. Then, the critical Bond and Ohnesorge numbers from section 2.2 already place some constrains upon the considered bubble size spectrum. The lower bound R_{Oh_1} for the size of a bubble is placed by the critical Ohnesorge number $Oh_1 = 0.038$. The upper bound for jet drop formation is given by $Bo \approx 3$ [12], but we already decided to neglect jet drop formation above $Bo \approx 0.1$, where the film drop mechanism dominates. Let R_{Bo} be the critical radius corresponding to $Bo = 0.1$.

We will consider the upper bound of bubble distribution to be given by the Hinze scale [13]

$$R_H = c(\sigma/\rho)^{3/5} \gamma_t^{-2/5}, \tag{83}$$

where c is a constant and γ_t is the turbulent dissipation rate experienced by a bubble moving through the liquid. A bubble with larger radius than the Hinze scale is likely to break up into smaller bubbles under turbulence [13]. We will use the estimated values $c = 0.363$ and $\gamma_t = 0.1$ W/kg [13] to calculate the Hinze scale.

3.2 Results

The critical radii introduced in section 3.1.1 are listed in table 3.2 for each organic compound. We see that in each case the Hinze scale R_H, which as the upper bound for our bubble radius, is less than the critical radius R_{Bo}. Thus we are always in the range $Bo < 0.1$ and considering jet drop production

only. In figures 5-9 we have calculated the organic mass percentages from equation (82) in the range $R_{Oh_1} - R_H$.

Table 1: The critical radii in meters for each organic compound, supersaturated cases in brackets

Compound	R_H	R_{Oh_1}	R_{Bo}
Benzyl alcohol	$1.8 \cdot 10^{-3}$	$8.3 \cdot 10^{-5}$	$6.7 \cdot 10^{-3}$
Benzoic acid	$3.1 \cdot 10^{-3}$	$3.1 \cdot 10^{-5}$	$1.0 \cdot 10^{-2}$
SRFA	$2.3 \cdot 10^{-3}$	$4.9 \cdot 10^{-5}$	$8.1 \cdot 10^{-3}$
Phenylalanine	$3.1 \cdot 10^{-3}$	$3.3 \cdot 10^{-5}$	$1.0 \cdot 10^{-2}$
Sodium phenylalanine	$3.1 \cdot 10^{-3}$	$4.0 \cdot 10^{-5}$	$1.0 \cdot 10^{-2}$
(Benzyl alcohol)	$6.4 \cdot 10^{-4}$	$5.0 \cdot 10^{-4}$	$2.8 \cdot 10^{-3}$
(Benzoic acid)	$3.1 \cdot 10^{-3}$	$3.3 \cdot 10^{-5}$	$1.0 \cdot 10^{-2}$
(Phenylalanine)	$3.0 \cdot 10^{-3}$	$4.4 \cdot 10^{-5}$	$1.0 \cdot 10^{-2}$
(Sodium phenylalanine)	$2.9 \cdot 10^{-3}$	$9.3 \cdot 10^{-5}$	$1.0 \cdot 10^{-2}$

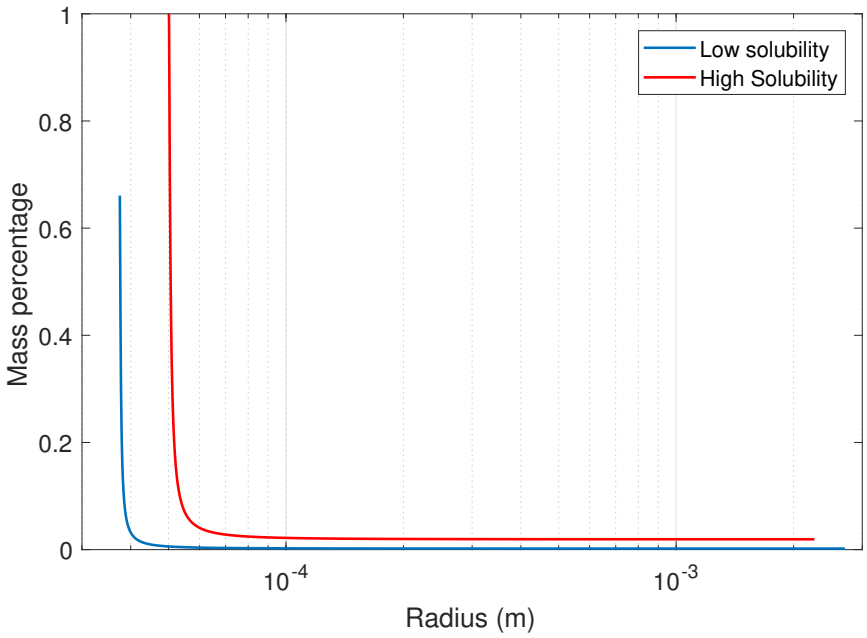

Figure 5: Mass percentage of SRFA in jet drops as a function of bursting bubble radius. Corresponding jet drop radius range (m): $5.2 \cdot 10^{-10} - 3.7 \cdot 10^{-4}$ (supersaturated: $1.2 \cdot 10^{-9} - 2.7 \cdot 10^{-4}$)

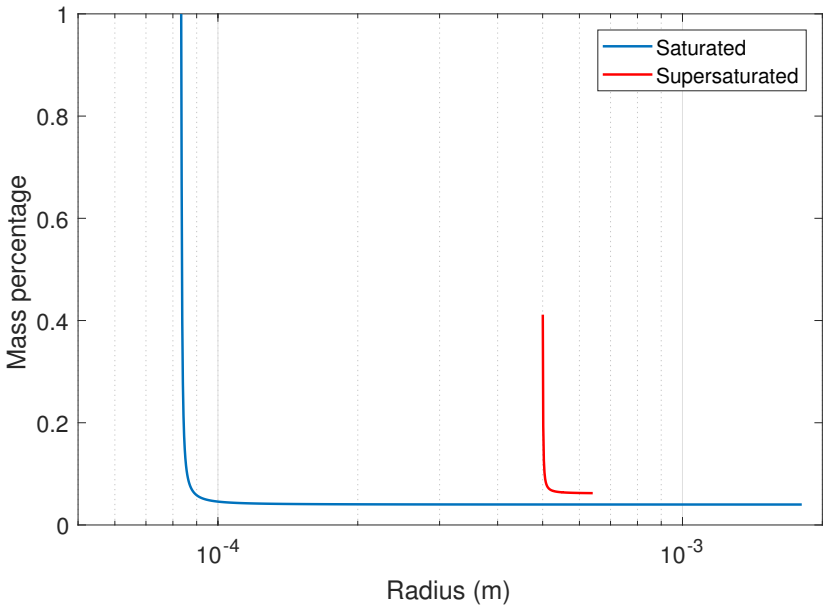

Figure 6: Mass percentage of benzyl alcohol in jet drops as a function of bursting bubble radius. Corresponding jet drop radius range (m): $7.3{\cdot}10^{-10}$ – $1.8 \cdot 10^{-4}$ (supersaturated: $5.0 \cdot 10^{-9} - 3.4 \cdot 10^{-6}$)

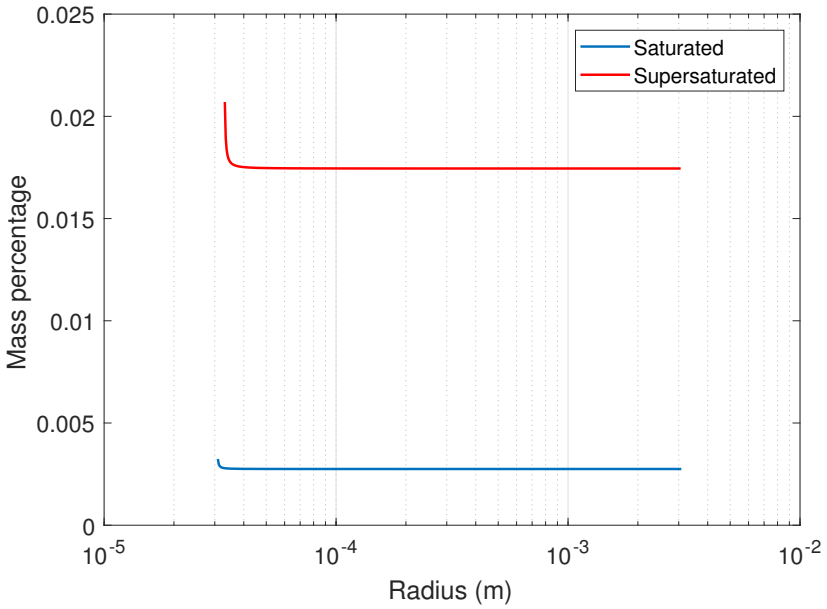

Figure 7: Mass percentage of benzoic acid in jet drops as a function of bursting bubble radius. Corresponding jet drop radius range (m): $6.0{\cdot}10^{-10}$ – $4.5 \cdot 10^{-4}$ (supersaturated: $5.8 \cdot 10^{-10} - 4.4 \cdot 10^{-4}$)

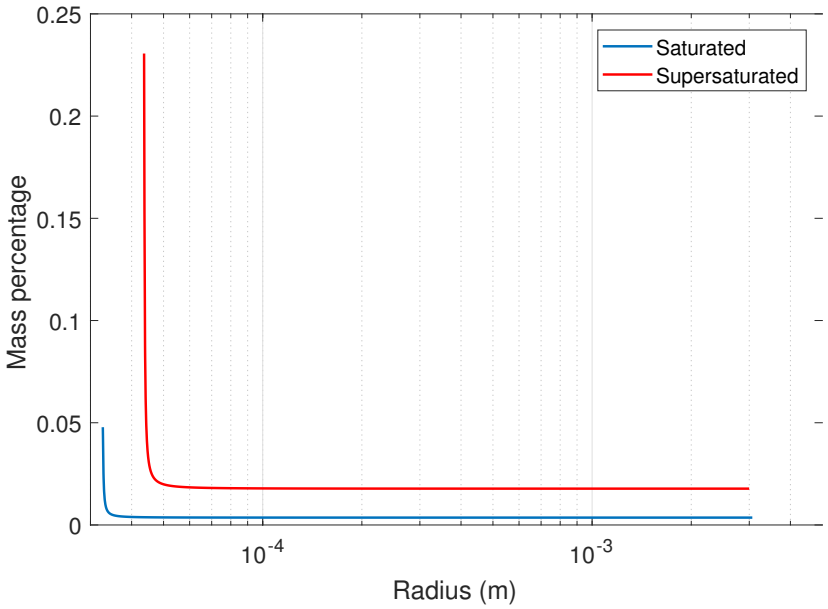

Figure 8: Mass percentage of phenylalanine in jet drops as a function of bursting bubble radius. Corresponding jet drop radius range (m): $4.4{\cdot}10^{-10}-4.4\cdot10^{-4}$ (supersaturated: $4.2\cdot10^{-10}-4.1\cdot10^{-4}$)

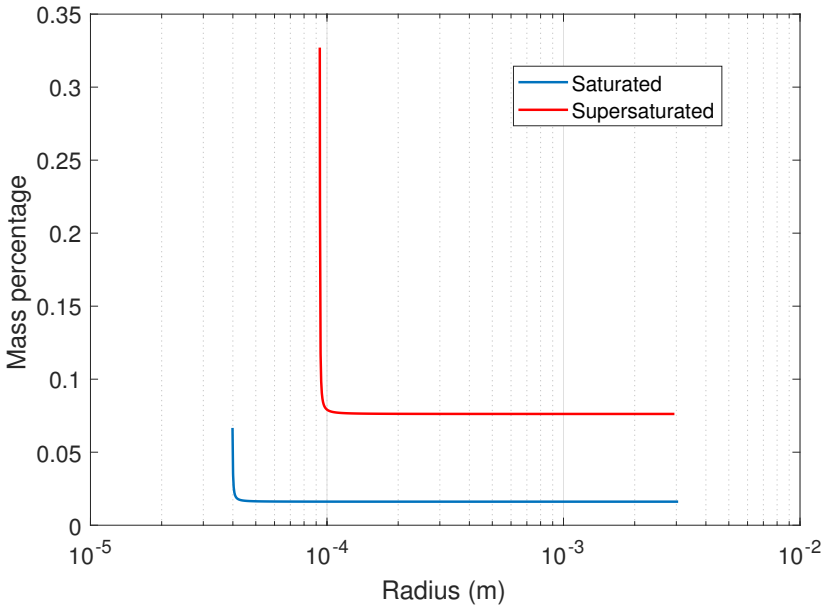

Figure 9: Mass percentage of sodium phenylalanine in jet drops as a function of bursting bubble radius. Corresponding jet drop radius range (m): $6.2\cdot10^{-10}-4.2\cdot10^{-4}$ (supersaturated: $4.4\cdot10^{-10}-3.3\cdot10^{-4}$)

In each curve we can identify two regions. In the immediate vicinity of the critical radius R_{Oh_1}, the organic is enriched compared to the bulk concentration. This is because the jet drop radius becomes comparable to the surface layer thickness, and thus the composition of the entire drop approaches the surface layer composition. This is most clearly seen in figure 6. In these cases, when the droplet is composed entirely or mostly of the surface layer, the accuracy of our calculation is determined by the accuracy of the chosen surface layer model, the monolayer model in this work.

The surface mole fraction of benzyl alcohol, as calculated from the monolayer model, is equal to one in both the saturated and supersaturated cases. In the saturated case the drop radius becomes equal to the surface thickness and we have a droplet composed entirely of benzyl alcohol (similar behavior is seen in the high solubility case for SRFA.) In the supersaturated case the surface layer is still entirely benzyl alcohol, but the surface layer thickness has become significantly smaller than the drop radius and we have a mass percentage of roughly 40%.

As the bursting bubble radius increases, the drop composition very quickly becomes nearly equal to the bulk composition, as the surface layer thickness becomes insignificant compared to the size of the jet drop. In light of this behavior, any uncertainties in the value of the Hinze scale due to γ_t become irrelevant, as long as $R_H \gg R_{Oh_1}$.

In figures 10-13 we have calculated four systems, the saturated and supersaturated cases according to table 3, at high and low bubble radii, showing the mass percentage of each component in the system.

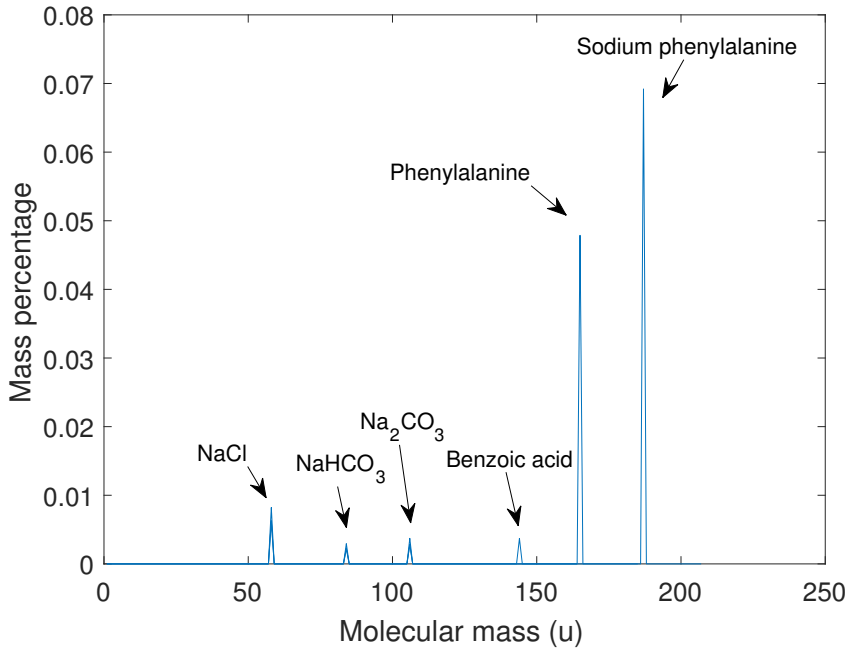

Figure 10: Saturated system, calculated at the critical radius R_{Oh1}

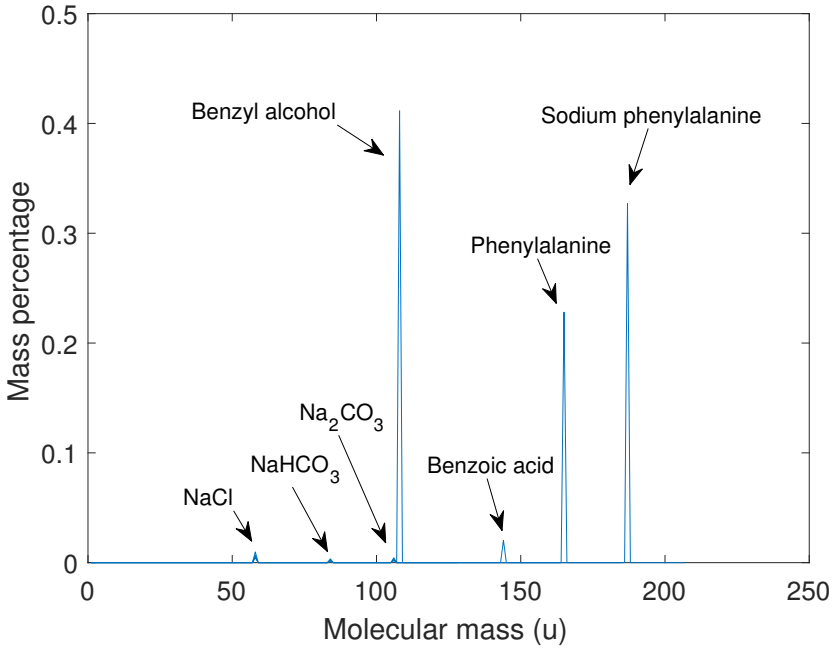

Figure 11: Supersaturated system, calculated at the critical radius R_{Oh1}

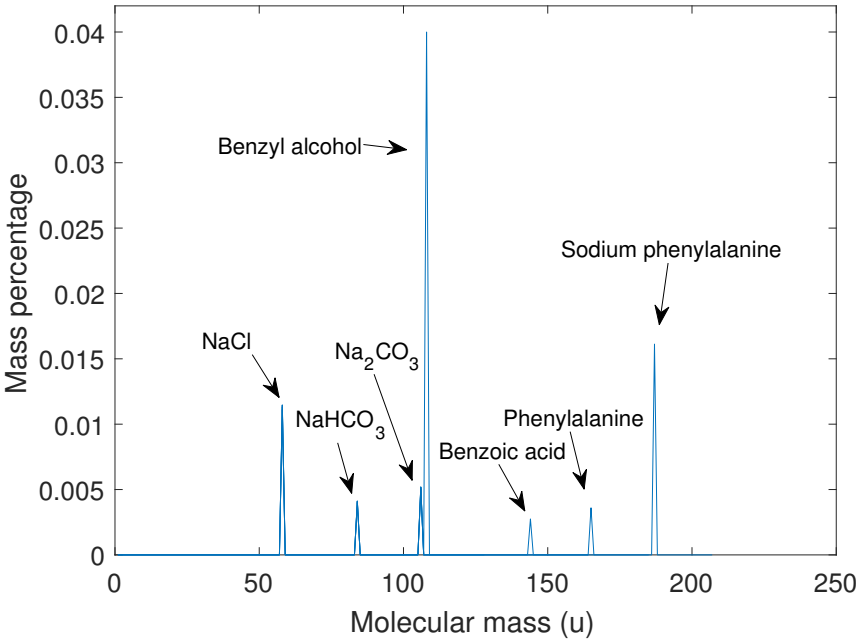

Figure 12: Saturated system, calculated at the Hinze scale R_H

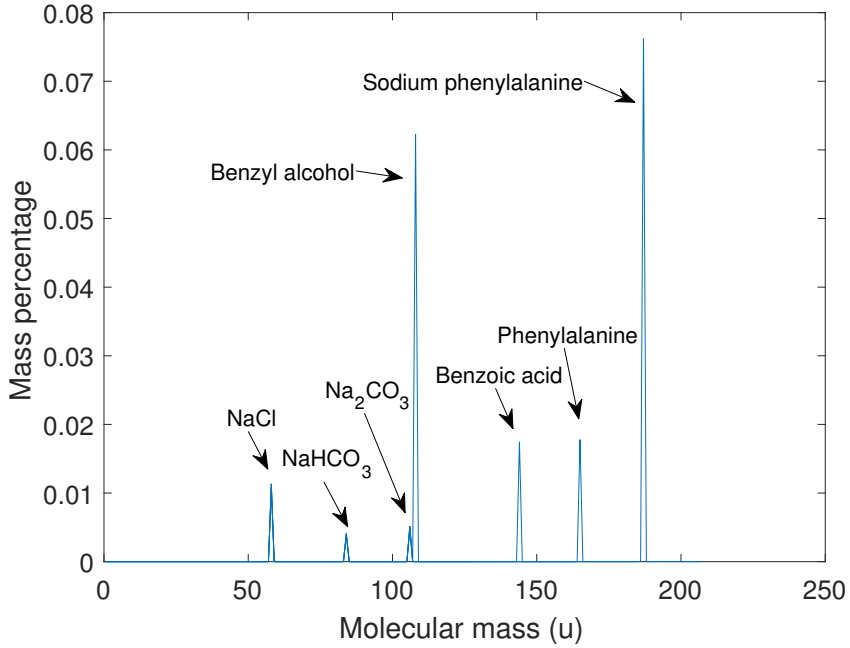

Figure 13: Supersaturated system, calculated at the Hinze scale R_H

The latter two figures are calculated at the Hinze scale, but due to the behavior seen in figures 5-9 these figures essentially describe droplets with bulk ocean composition and could be produced from any bursting bubble with a radius suitably larger than the critical radius R_{Oh_1}. Indeed such droplets would be produced by film drops as well, if bubbles larger than the Hinze scale are present. Figures 10 and 11 are calculated at the critical radius and should be seen the upper limit for each compound. Benzyl alcohol, whose mass percentage goes to one in the saturated case, is omitted from figure 10. The mass percentages of SRFA are 100% and 65% at the critical radius, and 1.9% and 0.2% at the Hinze scale, for the high and low solubility cases respectively.

One should note that the organic compounds are treated separately and do not interact with each other. The figures 10-13 are combined plots from separate calculations. The salt mass percentages do not vary greatly between different different organic compounds considered, and are layered on top of each other in the figures.

Our calculations describe droplets right after their formation. As the droplets rise to the moon's surface, their water content is liable to change due to condensation from the surrounding vapor [2]. The total amount of salt and organics in the droplets however should stay the same. In the Cassini measurements, the ratio of the benzene cation peak to the high-mass organic cation (HMOC) peaks is roughly 3:1 [2]. In our calculations this would correspond to the ratio of SRFA to the rest of the organic compounds. The system that best matches this ratio is the one seen in figure 12, with $(w_{NaPhe} + w_{Phe} + w_{BnA} + w_{BnOH})/w_{SRFA} \approx 3.3$, if one chooses the high solubility estimate for SRFA.

Comparing the sodium peaks to the organic peaks in [2], we see that there is roughly twice as much salt in the ice grains than organic compounds. None of our calculated systems contain this much salt compared to the organics. The surface concentrations of the salts as calculated from the monolayer model are roughly 60% of the bulk concentration. This behavior is consistent with experiments [14, 15]. If some of our calculated systems contained high amounts of salts, this discrepancy could be explained by a bubble size spectrum that suitably emphasised those bubble sizes. However, the organic mass percentages are much higher than the salt mass percentages in every system, including the systems calculated at the Hinze scale. Thus, no bubble size spectrum could produce a system of ice grains with overall more salt than organics. This implies that by assuming saturation concentrations in

the ocean we have introduced too much organic material into the system from the beginning, and the bulk organic concentrations should perhaps be lower than saturation. However, our model neglects any aerosol dynamical processes the droplets might experience as they travel through the plume gas to the surface, which could explain the discrepancy.

4 Conclusions

By combining the scaling laws of film and jet drops with a surface monolayer model, we have produced a method for estimating the chemical compositions of bubble bursting aerosols. We have applied this method to Enceladus' plume ice grains which are known to contain organic compounds, but the method has great generality and could be applied to any terrestrial or extraterrestrial system where bubble bursting aerosols might be found. The model predicts the strong enrichment of small droplets containing surface active compounds. The calculated droplets contain lower amounts of salts than organic compounds, in contrast with Cassini measurements.

Characterization of the surface layer is essential to obtaining the composition of a droplet. The calculations could be performed using a different surface layer model than the monolayer model used here. The calculations could be improved by more sophisticated estimates for mixture surface tensions and viscosities, and a better understanding of the ocean water composition. Results are also hindered by a poor knowledge of the bursting bubble size distribution. Future models could account for aerosol dynamics as the droplets travel from the ocean-gas interface to the moon's surface.

A Appendix: Surface tensions, viscosities, densities and solubilities

Water

The surface tension of water (N/m) is given by the following equation [16]

$$\sigma_w(T) = 0.2358\left(\frac{647.096 - T}{647.096}\right)^{1.256}\left(1 - 0.625\frac{647.096 - T}{647.096}\right), \tag{84}$$

in the range $273\,\mathrm{K} < T < 380\,\mathrm{K}$.

The viscosity of water (mPa s) is given by [17]

$$\mu_w(t) = \frac{t + 243}{0.05594t^2 + 5.2842t + 137.37}, \tag{85}$$

in the range $0°\mathrm{C} < t < 150°\mathrm{C}$.

The density of water (g/cm^3) is given by [18]

$$\rho_w(T) = 0.08\tanh\left(\frac{T - 225}{46.2}\right) + 0.7415\left(\frac{647.096 - T}{647.096}\right)^{0.33} + 0.32. \tag{86}$$

Sodium chloride

The extrapolated surface tension (N/m) of supercooled NaCl is given by [11]

$$\sigma_{NaCl}(T) = 0.19116 - 0.07188 \cdot 10^{-3}T. \tag{87}$$

The surface tension of a binary water + salt mixture is given by [11]

$$\sigma = \sigma_w + \chi_s F_{ws}(T), \tag{88}$$

where χ_s is the mole fraction of the salt and

$$F_{ws}(T) = a + bT. \tag{89}$$

The surface tension of a mixture of N components is then given by [11]

$$\ln\sigma = \sum_i^N \chi_i \ln\left(\sigma_i(T) + \sum_j^N \chi_j F_{ij}(T)\right), \tag{90}$$

which is a modified version of equation (72). See table 2 for the fitting parameters a and b for each compound.
The extrapolated density (kg/m^3) of liquid NaCl, based on, is given by [19]

$$\rho_{NaCl} = (2.1389 - 0.5426 \cdot 10^{-3}T). \tag{91}$$

The relative viscosity $\mu_r = \mu_s/\mu_w$ of NaCl solution is given by Zhang and Han [20].

Sodium carbonate and sodium bicarbonate

The extrapolated surface tensions of supercooled sodium carbonate and bicarbonate, and their model parameters a and b are given by Dutcher et al. [11], see Table 2.

The densities of supercooled molten sodium carbonate and bicarbonate are extrapolated from the data given by Janz [19]. The densities of aqueous sodium carbonate and bicarbonate solutions are given by [21]. The density of a salt water mixture with, sodium chloride, sodium carbonate and sodium bicarbonate is given by the model of Potter and Haas [22].

The viscosity (mPa s) of a sodium carbonate and bicarbonate solution is given by the following fit

$$\mu(t) = 1.8113 - 0.0229t, \tag{92}$$

made to values provided by [23].

Organic compounds

The surface tension of pure benzyl alcohol is calculated from a fit given by [24]. The surface tension of pure benzoic acid is extrapolated from the values given by [25].

The Dutcher model parameters are listed in the table below.

Table 2: Dutcher model parameters

	a (mN m^{-1})	b (mN $m^{-1}K^{-1}$)	Source
Benzyl alcohol	-8824.6	8.7	[26]
Benzoic acid	-267.7	-	[27]
Phenylalanine	988.9	-9.4	[28]
Sodium phenylalanine	693.8	-4.6	[29]
NaCl	232.5	-0.25	[11]
$NaHCO_3$	46.4	-	[11]
Na_2CO_3	56.0	-	[11]

The surface tensions of pure phenylalanine and sodium phenylalanine are set to 60 mN/m, as an estimate based on their aqueous solutions [28, 29]. For SRFA, we replace the second term in equation (88) with the logarithmic term in the Szyszkowski equation [30]. The surface tension of pure SRFA is set to 50 mN/m, again as a guess based on the aqueous solution surface tension [30].

The viscosity of benzyl alcohol at 0 °C is extrapolated from values given by [31]. The relative viscosity of benzoic acid is described by [32]. We assume the relative viscosity of SRFA to be negligible. See [33] for the relative viscosity of a fulvic acid, which is seen to be a complicated function of concentration, but with a small value. See [34] for the relative viscosity of phenylalanine solutions, which we also use for sodium phenylalanine. We calculate the viscosity of a mixture by first multiplying the viscosity of water with known relative viscosities and then using equation (73).

The density of phenylalanine and sodium phenylalanine is estimated to be 1.227 g/cm^3 using E-AIM [1] [35, 36]. The (effective) density of SRFA is 1.5 g/cm^3 [37]. The density of benzyl alcohol is given by [24]. The density of benzoic acid is given by [38].

The solubility of SRFA in water is 2-3 g/l, further increasing linearly up to 20 g/l as more SRFA is added to the system [39]. This gives us the high and low solubilities seen in table 3. The solubilities of benzoic acid and benzyl alcohol at room temperature are 3.44 g/l [31] and 40 g/l [40] respectively. Their temperature dependence from 0°C to 100°C was estimated using COSMOtherm[2] [41, 42], giving the values seen in Table 3. The solubility of phenylalanine in water is given by [43], where phenylalanine is highly dissociated due to the high pH on Enceladus.

[1] http://www.aim.env.uea.ac.uk/aim/aim.php

[2] http://www.cosmologic.de

Table 3: Solubilities of the organic compounds in mole fractions

Compound	0 °C	100 °C
Benzyl alcohol	0.007	0.011
Benzoic acid	0.00035	0.00225
SRFA (high)	0.0006	-
SRFA (low)	0.00006	-
Phenylalanine	0.0004	0.002
Sodium phenylalanine	0.0016	0.008

References

[1] C. R. Glein, J. A. Baross, and J. H. Waite. The pH of Enceladus' ocean. *Geochimica et Cosmochimica Acta*, 162:202–219, 2015.

[2] F. Postberg, N. Khawaja, B. Abel, G. Choblet, C. R. Glein, M. S. Gudipati, B. L. Henderson, H.W. Hsu, S. Kempf, F. Klenner, et al. Macromolecular organic compounds from the depths of Enceladus. *Nature*, 558(7711):564, 2018.

[3] F. Veron. Ocean Spray. *Annual Review of Fluid Mechanics*, 47(1):507–538, 2015.

[4] H. Lhuissier and E. Villermaux. Bursting bubble aerosols. *Journal of Fluid Mechanics*, 696:5–44, 2012.

[5] A. M. Gañán Calvo. Scaling laws of top jet drop size and speed from bubble bursting including gravity and inviscid limit. *Physical Review Fluids*, 3:091601, 2018.

[6] J. Malila and N. L. Prisle. A Monolayer Partitioning Scheme for Droplets of Surfactant Solutions. *Journal of Advances in Modeling Earth Systems*, 10(12):3233–3251, 2018.

[7] S. Olsztyńska-Janus, M. Komorowska, L. Vrielynck, and N. Dupuy. Vibrational Spectroscopic Study of L-Phenylalanine: Effect of pH. *Applied Spectroscopy*, 55, 2001.

[8] R. A. Jacobson, P. G. Antreasian, J. J. Bordi, K. E. Criddle, R. Ionasescu, J. B. Jones, R. A. Mackenzie, M. C. Meek, D. Parcher, F. J. Pelletier, Jr. W. M. Owen, D. C. Roth, I. M. Roundhill, and J. R. Stauch. The Gravity Field of the Saturnian System from Satellite Observations and Spacecraft Tracking Data. *The Astronomical Journal*, 132(6):2520–2526, 2006.

[9] L. D. Landau and E. M. Lifshitz. *Fluid mechanics*. Course of theoretical physics. Pergamon Press, Oxford, 1959.

[10] C.Y. Lai, J. Eggers, and L. Deike. Bubble Bursting: Universal Cavity and Jet Profiles. *Physical Review Letters*, 121:144501, 2018.

[11] C. S. Dutcher, A. S. Wexler, and S. L. Clegg. Surface Tensions of Inorganic Multicomponent Aqueous Electrolyte Solutions and Melts. *The Journal of Physical Chemistry A*, 114(46):12216–12230, 2010.

[12] P. L. L. Walls, L. Henaux, and J. C. Bird. Jet drops from bursting bubbles: How gravity and viscosity couple to inhibit droplet production. *Physical Review E*, 92:021002, 2015.

[13] C. Garrett, M. Li, and D. Farmer. The Connection between Bubble Size Spectra and Energy Dissipation Rates in the Upper Ocean. *Journal of Physical Oceanography*, 30(9):2163–2171, 2000.

[14] P. Jungwirth and D. J. Tobias. Specific Ion Effects at the Air/Water Interface. *Chemical Reviews*, 106(4):1259–1281, 2006.

[15] W. Hua, X. Chen, and H. C. Allen. Phase-Sensitive Sum Frequency Revealing Accommodation of Bicarbonate Ions, and Charge Separation of Sodium and Carbonate Ions within the Air/Water Interface. *The Journal of Physical Chemistry A*, 115(23):6233–6238, 2011.

[16] V. Holten, D. G. Labetski, and M. E. H. van Dongen. Homogeneous nucleation of water between 200 and 240 K: New wave tube data and estimation of the Tolman length. *The Journal of Chemical Physics*, 123(10):104505, 2005.

[17] M. Laliberté. Model for Calculating the Viscosity of Aqueous Solutions. *Journal of Chemical & Engineering Data*, 52(2):321–335, 2007.

[18] J. Wölk and R. Strey. Homogeneous Nucleation of H_2O and D_2O in Comparison: The Isotope Effect. *The Journal of Physical Chemistry B*, 105(47):11683–11701, 2001.

[19] G.J. Janz. *Thermodynamic and Transport Properties for Molten Salts: Correlation Equations for Critically Evaluated Density, Surface Tension, Electrical Conductance, and Viscosity Data*. Number v. 17 in Journal of physical and chemical reference data. American Chemical Society and the American Institute of Physics, 1988.

[20] Zhang and Han. Viscosity and Density of Water + Sodium Chloride + Potassium Chloride Solutions at 298.15 K. *Journal of Chemical & Engineering Data*, 41(3):516–520, 1996.

[21] J. P. Hershey, S Sotolongo, and F. J. Millero. Densities and compressibilities of aqueous sodium carbonate and bicarbonate from 0° to 45° C. *Journal of Solution Chemistry*, 12(4):233–254, 1983.

[22] Potter R. W., II and Haas J. L., Jr. Models for calculating density and vapor pressure of geothermal brines. *Journal of Research of the U. S. Geological Survey*, 6:247–257, 1978.

[23] G. Vázquez, E. Alvarez, and J. M. Navaza. Density, Viscosity, and Surface Tension of Sodium Carbonate + Sodium Bicarbonate Buffer Solutions in the Presence of Glycerine, Glucose, and Sucrose from 25 to 40 °C. *Journal of Chemical & Engineering Data*, 43(2):128–132, 1998.

[24] K.D. Chen, Y.F. Lin, and C.H. Tu. Densities, Viscosities, Refractive Indexes, and Surface Tensions for Mixtures of Ethanol, Benzyl Acetate, and Benzyl Alcohol. *Journal of Chemical & Engineering Data*, 57(4):1118–1127, 2012.

[25] F. D. Snell, editor. *Encyclopedia of industrial chemical analysis. Vol. 7, Benzene to brewery products*. Interscience Publishers, New York (N.Y.), 1968.

[26] J. Glinski, G. Chavepeyer, and J.K. Platten. Surface properties of dilute aqueous solutions of cyclohexyl and benzyl alcohols and amines. *New journal of chemistry*, 19(11):1165–1170, 1995.

[27] B. Minofar, P. Jungwirth, M. R. Das, W. Kunz, and S. Mahiuddin. Propensity of formate, acetate, benzoate, and phenolate for the aqueous solution/vapor interface: Surface tension measurements and molecular dynamics simulations. *The Journal of Physical Chemistry C*, 111(23):8242–8247, 2007.

[28] A. Chandra, V. Patidar, M. Singh, and R Kale. Physicochemical and friccohesity study of glycine, L-alanine and L-phenylalanine with aqueous methyltrioctylammonium and cetylpyridinium chloride from $T =$ (293.15 to 308.15) K. *The Journal of Chemical Thermodynamics*, 65:18–28, 2013.

[29] S. Garg, Dr Mohd Shariff, M. Shaikh, B. Lal, S. Ahmed, and N. Faiqa. Surface Tension and Derived Surface Thermodynamic Properties of

Aqueous Sodium Salt of L-Phenylalanine. *Indian Journal of Science and Technology*, 9, 2016.

[30] E. Aumann, L.M. Hildemann, and A. Tabazadeh. Measuring and modeling the composition and temperature-dependence of surface tension for organic solutions. *Atmospheric Environment*, 44(3):329 – 337, 2010.

[31] J. R. Rumble, editor. *CRC Handbook of Chemistry and Physics, 99th Edition (Internet Version 2018)*. CRC Press/Taylor & Francis, Boca Raton, FL.

[32] P.K. Mandal, D.K. Chatterjee, B.K. Seal, and A.S. Basu. Viscosity behavior of benzoic acid and benzoate ion in aqueous solution. *Journal of Solution Chemistry*, 7(1):57–62, 1978.

[33] F. Rey, M.A. Ferreira, P. Facal, and A.A.S.C. Machado. Effect of concentration, pH, and ionic strength on the viscosity of solutions of a soil fulvic acid. *Canadian Journal of Chemistry*, 74(3):295–299, 1996.

[34] Riyazuddeen and S. Afrin. Viscosities of l-Phenylalanine, l-Leucine, l-Glutamic Acid, or l-Proline + 2.0 mol·dm^{-3} Aqueous NaCl or 2.0 mol·dm^{-3} Aqueous $NaNO_3$ Solutions at T = (298.15 to 328.15) K. *Journal of Chemical & Engineering Data*, 55(9):3282–3285, 2010.

[35] S. L. Clegg and A. S. Wexler. Densities and Apparent Molar Volumes of Atmospherically Important Electrolyte Solutions. 1. The Solutes H_2SO_4, HNO_3, HCl, Na_2SO_4, $NaNO_3$, NaCl, $(NH_4)_2SO_4$, NH_4NO_3, and NH_4Cl from 0 to 50 °C, Including Extrapolations to Very Low Temperature and to the Pure Liquid State, and $NaHSO_4$, NaOH, and NH_3 at 25 °C. *The Journal of Physical Chemistry A*, 115(15):3393–3460, 2011.

[36] S. L. Clegg and A. S. Wexler. Densities and Apparent Molar Volumes of Atmospherically Important Electrolyte Solutions. 2. The system H^+ - HSO_{4^-} - SO_4^{2-} - H_2O from 0 - 3 mol kg^{-1} as a function of temperature and H^+ - NH_{4^+} - HSO_{4^-} - SO_4^{2-} - H_2O from 0 - 6 mol kg^{-1} at 25 °C using a Pitzer ion interation model, and NH_4HSO_4 - H_2O and $(NH_4)_3H(SO_4)_2$ - H_2O over the entire concentration range. *The Journal of Physical Chemistry A*, 115(15):3461–3474, 2011.

[37] E. Dinar, T. F. Mentel, and Y. Rudich. The density of humic acids and humic like substances (HULIS) from fresh and aged wood burning and pollution aerosol particles. *Atmospheric Chemistry and Physics*, 6(12):5213–5224, 2006.

[38] T. Sun and A. S. Teja. Density, Viscosity, and Thermal Conductivity of Aqueous Benzoic Acid Mixtures between 375 K and 465 K. *Journal of Chemical & Engineering Data*, 49(6):1843–1846, 2004.

[39] I. Salma, R. Ocskay, and G. G. Láng. Properties of atmospheric humic-like substances &; water system. *Atmospheric Chemistry and Physics*, 8(8):2243–2254, 2008.

[40] *Kirk-Othmer encyclopedia of chemical technology. Volume 4, Bearing materials to Carbon.* John Wiley & Sons, New York N.Y., 4. edition, 1992.

[41] COSMOtherm, 18.0.1, COSMOlogic GmbH & Co KG.

[42] F. Eckert and A. Klamt. Fast solvent screening via quantum chemistry: COSMO-RS approach. *AIChE Journal*, 48:369 – 385, 2002.

[43] P. Ji and W. Feng. Solubility Of Amino Acids In Water And Aqueous Solutions By the Statistical Associating Fluid Theory. *Industrial & Engineering Chemistry Research*, 47(16):6275–6279, 2008.